

# Diffusion and Volume Maximization-Based Clustering of Highly Mixed Hyperspectral Images

Sam L. Polk<sup>1</sup>, Kangning Cui<sup>2</sup>, Robert J. Plemmons<sup>3</sup>, and James M. Murphy<sup>\*1</sup>

<sup>1</sup> Department of Mathematics, Tufts University

<sup>2</sup> Department of Mathematics, City University of Hong Kong

<sup>3</sup> Departments of Mathematics and Computer Science, Wake Forest University

## Abstract

Hyperspectral images of a scene or object are a rich data source, often encoding a hundred or more spectral bands of reflectance at each pixel. Despite being very high-dimensional, these images typically encode latent low-dimensional structure that can be exploited for material discrimination. However, due to an inherent trade-off between spectral and spatial resolution, many hyperspectral images are generated at a coarse spatial scale, and single pixels may correspond to spatial regions containing multiple materials. This article introduces the *Diffusion and Volume maximization-based Image Clustering (D-VIC)* algorithm for unsupervised material discrimination. D-VIC locates cluster modes—high-density, high-purity pixels in the hyperspectral image that are far in diffusion distance (a data-dependent distance metric) from other high-density, high-purity pixels—and assigns these pixels unique labels, as these points are meant to exemplify underlying material structure. Non-modal pixels are labeled according to their diffusion distance nearest neighbor of higher density and purity that is already labeled. By directly incorporating pixel purity into its modal and non-modal labeling, D-VIC upweights pixels that correspond to a spatial region containing just a single material, yielding more interpretable clusterings. D-VIC is shown to outperform baseline and comparable state-of-the-art methods in extensive numerical experiments on a range of hyperspectral images, implying that it is well-equipped for material discrimination and clustering of these data.

**Index Terms:** Clustering, Diffusion Geometry, Graphs, Hyperspectral Imaging, Image Segmentation, Machine Learning, Spectral Unmixing, Unsupervised Learning.

## 1 Introduction

Hyperspectral images (HSIs) are images of a scene or object, encoding reflectance at a hundred or more spectral bands per pixel [Eis12, GPC<sup>+</sup>17, PMP<sup>+</sup>11]. HSI remote sensing data, which is generated continuously by airborne and orbital sensors, has been successfully used for material discrimination in fields ranging from forensic medicine (e.g., age estimation of forensic traces [EGVL<sup>+</sup>12]), conservation (e.g., species mapping in wetlands [AMR10, HMW03]), and ecology (e.g., estimating water content in vegetation canopies [CKS10]). The high dimensional characterization of a scene provided in remote sensing HSI data has motivated its use in the *material discrimination* problem [DBG08], wherein machine learning algorithms are meant to separate pixels based on the constituent materials in the spatial region they correspond to [GPC<sup>+</sup>17, PMP<sup>+</sup>11].

Though hyperspectral imagery has become an essential tool across many scientific domains, material discrimination using HSI data faces at least two key difficulties. First, because of an inherent trade-off between spectral and spatial resolution, HSIs are typically generated at coarse spatial resolution [JWC<sup>+</sup>20, Pri97, BDPCV<sup>+</sup>13, LSR15]. One would prefer an HSI with both a high spatial resolution (so that individual pixels correspond to spatial regions containing just one material) and a high spectral resolution (to enable capacity for material discrimination) [Pri97]. However, an increase in the spatial resolution of an HSI often

<sup>\*</sup>Corresponding Author: JM.Murphy@Tufts.edu

comes at the cost of reducing the effective detection energy entering the recording spectrometer across each spectral band [JWC<sup>+</sup>20]. While this effect may be mitigated at least partially by increasing the aperture of the optical system underlying the spectrometer used to generate HSI data [JWZ<sup>+</sup>17], high-aperture instruments generally also have high volume and weight [JWC<sup>+</sup>20]. As such, HSI data is generated at a coarse spatial resolution (often as high as 20 m per pixel). Thus, though some *high-purity* pixels in an HSI may correspond to spatial regions containing predominantly just one material, other pixels are mixed: corresponding to spatial regions with many distinct materials.

Second, expert labeling to generate training data for supervised machine learning is often impractical due to the large quantities of HSI data continuously generated by remote sensors [Eis12]. To efficiently analyze unlabeled HSIs, one may use HSI clustering algorithms, which partition HSI pixels into groups of points sharing key commonalities [FHT01]. These algorithms are *unsupervised* i.e., ground truth labels are not needed to provide a partition of an HSI [FHT01]. Clustering is usually one of the first tools available to a user interested in exploring a new dataset. Though clustering has become an important tool in the field of hyperspectral imagery [MM18, AG21, ZWL<sup>+</sup>16, KDP12, WNW<sup>+</sup>19, CVMZ07, GJC<sup>+</sup>14, WP17, YYL<sup>+</sup>18, NMI<sup>+</sup>20, GKP14, LQL<sup>+</sup>21, SWW<sup>+</sup>20], clustering algorithms that do not directly account for the fact that HSI pixels are often spectrally mixed may fail to extract meaningful latent cluster structure. Thus, efficient unsupervised machine learning algorithms incorporating pixel purity into their labeling are needed to analyze the rich material structure encoded in HSI data [CP21].

This article introduces the *Diffusion and Volume maximization-based Image Clustering (D-VIC)* algorithm for unsupervised material discrimination of HSIs. D-VIC is the first algorithm to simultaneously exploit the high-dimensional geometry [BAF05, AG21] and abundance structure [CP21, BDPCV<sup>+</sup>13] observed in HSIs for the clustering problem. In its first stage, D-VIC locates cluster modes: high-purity, high-empirical density pixels that are far in diffusion distance (a data-dependent distance metric [CL06]) from other high-purity, high-density pixels. These pixels serve as exemplars for all underlying material structure in the HSI. In its mode selection, D-VIC downweights high-density pixels that correspond to commonly co-occurring groups of materials. As such, D-VIC’s exploitation of spectrally mixed structure in HSI data [JWC<sup>+</sup>20, Pri97, BDPCV<sup>+</sup>13, LSR15, BDPCV<sup>+</sup>13] enables the selection of modes that better represent the material structure in the scene.

After detecting cluster modes, D-VIC propagates modal labels to non-modal pixels in order of decreasing density and pixel purity. Since pixel purity is also incorporated into D-VIC’s non-modal labeling, D-VIC accounts for material abundance structure in the HSI during its entire labeling procedure. D-VIC is compared against classical and related state-of-the-art HSI clustering algorithms on three benchmark real HSI datasets and one synthetic dataset built to demonstrate the key strengths of D-VIC. On each dataset, D-VIC produces a partition closer to the ground truth than related methods, and moreover enjoys robustness to parameter selection. Computationally, the proposed algorithm scales quasilinearly in the size of the HSI, and the empirical runtime of D-VIC is competitive, suggesting it is well-equipped to cluster large HSIs.

## 2 Background

### 2.1 Background on Unsupervised HSI Clustering

HSI clustering algorithms partition an HSI, denoted  $X = \{x_i\}_{i=1}^n \subset \mathbb{R}^D$  (interpreted as a point cloud of spectral signatures, with  $n$  pixels and  $D$  spectral bands) into  $K$  *clusters* of pixels. The partition, which we call a *clustering* of  $X$ , may be encoded in a labeling vector  $\mathcal{C} \in \{1, 2, \dots, K\}^n$  such that  $\mathcal{C}(x_i) = \mathcal{C}_i \in \{1, 2, \dots, K\}$  is the label assigned to the pixel  $x_i$ . Ideally, pixels from any one cluster are in some sense “related,” and pixels from any two clusters are “unrelated.” The exact notion of relatedness varies widely in the clustering literature [FHT01, NJW02, MM19b, GKP14]. Clustering algorithms are *unsupervised*, meaning that data points are labeled without the aid of any expert annotations or ground truth labels. This has motivated the development of clustering algorithms explicitly built for material discrimination using HSIs [MM18, AG21, ZWL<sup>+</sup>16, KDP12, WNW<sup>+</sup>19, CVMZ07, GJC<sup>+</sup>14, WP17, YYL<sup>+</sup>18, NMI<sup>+</sup>20, GKP14, LQL<sup>+</sup>21, SWW<sup>+</sup>20, CCM14].

Though classical clustering algorithms such as  $K$ -Means and the Gaussian Mixture Model (GMM) [FHT01] remain widely used in practice, these algorithms tend to perform poorly on HSIs for a number of reasons [MM18, AG21]. First, algorithms that rely on Euclidean distances are prone to the “curse of dimensionality” on datasets like HSIs that have a high ambient dimension (i.e., the number of spectral bands is

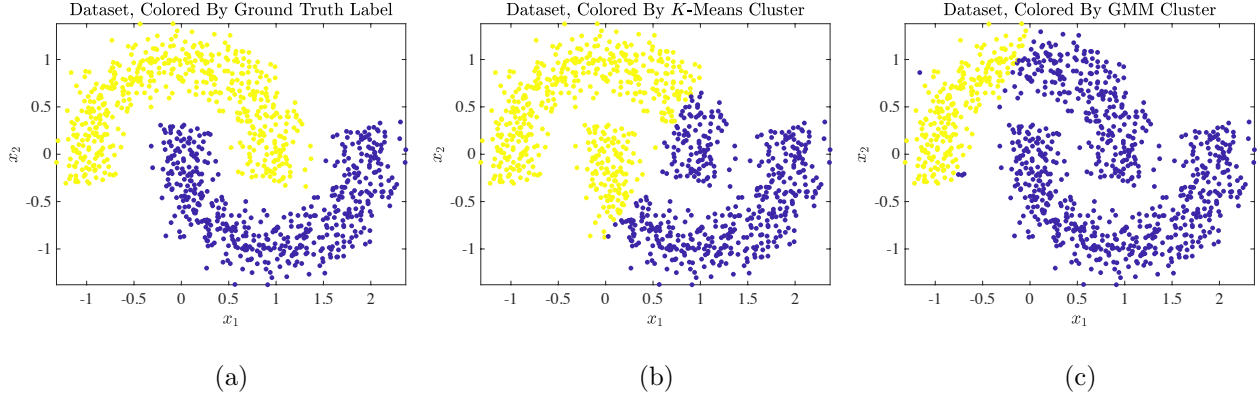


Figure 1: Example of a toy dataset ( $n = 1000$ ) with nonlinear cluster structure: two interleaving half-circles. The idealized clustering, visualized in (a), separates each half-circle. Due to the lack of a linear decision boundary, however, both  $K$ -Means ((b)) and GMM ((c)) were unable to extract latent cluster structure from this simple nonlinear dataset. Both algorithms were run with 100 replicates.

large) [TK06]. Second, HSIs are often spectrally mixed [JWC<sup>+</sup>20, Pri97, BDPCV<sup>+</sup>13, LSR15], and overlap may exist between clusters in Euclidean space [MM18]. A final complication is that classical algorithms generally assume that latent clusters in a dataset are approximately ellipsoidal groups of points that are well-separated in Euclidean space [FHT01], but clusters in HSIs often exhibit nonlinear structure. A simple toy dataset, visualized in Figure 1 [NJW02], serves as an example of dataset with nonlinear structure. This dataset lacks a linear decision boundary between its  $K = 2$  latent clusters, and classical algorithms ( $K$ -Means and GMM [FHT01]) were unable to learn its latent nonlinear cluster structure. HSIs often contain clusters that can only be separated using a nonlinear decision boundary [MM18]; thus, algorithms that rely solely on Euclidean distances are expected to perform poorly at material discrimination on HSIs.

The limitations outlined above have motivated the application and development of nonlinear graph-based algorithms for HSI clustering [AG21, ZWL<sup>+</sup>16, KDP12, ZCT<sup>+</sup>17, MM18, WNW<sup>+</sup>19, CVMZ07, GJC<sup>+</sup>14, NJW02, CCM14]. Graph-based algorithms rely on data-generated graphs; pixels are represented as nodes in the graph, and edges encode pairwise similarity between them. Highly connected regions in the graph may then be summarized using a nonlinear coordinate transformation [TdSL00, RS00, BN01, CL06], as is described in more detail in Section 2.2. Thus, a partition may be obtained by implementing a classical clustering algorithm on the dimension-reduced dataset. Graph-based clustering algorithms enjoy a strong theoretical backing that has motivated their development for HSI clustering [AG21, ZWL<sup>+</sup>16, KDP12, MM18, WNW<sup>+</sup>19, CVMZ07, GJC<sup>+</sup>14, CCM14]. For example, due to their reliance on a graph representation of an HSI, these algorithms tend to be robust to small perturbations in the data and noise. Moreover, theoretical guarantees exist for the successful recovery of latent cluster structure, even if boundaries between latent clusters are nonlinear [RCY11, MP22, MM19b]. Despite their exhibited successes, algorithms that rely solely on graph structure tend to perform poorly on datasets containing multimodal cluster structure [MM19b, MP22, NG07]; i.e., if a single cluster has multiple regions of high and low density. Importantly, this includes spectrally mixed HSIs, the classes of which often contain multiple co-occurring materials of varying abundances [JWC<sup>+</sup>20, Pri97, BDPCV<sup>+</sup>13].

Deep neural networks have recently become popular for material discrimination in HSIs because of their capacity for prediction on complex data sources like HSI [WP17, YYL<sup>+</sup>18, NMI<sup>+</sup>20, LQL<sup>+</sup>21, SWW<sup>+</sup>20]. While these algorithms tend to be highly accurate on real HSI data, many state-of-the-art deep models for HSI segmentation still rely on at least a small number of ground truth labels [WP17, YYL<sup>+</sup>18] and/or pseudo-labels [LQL<sup>+</sup>21, WP17]. Moreover, even fully unsupervised “deep clustering” algorithms [NMI<sup>+</sup>20, SWW<sup>+</sup>20] rely on deep neural networks, which are prone to error from perturbations and noise [NYC15, SZS<sup>+</sup>14], and whose strong performance in some settings may be incidental to the use of deep features [HYV20].

## 2.2 Background on Spectral Graph Theory

As overviewed in Section 2.1, graph-based clustering algorithms learn latent, possibly nonlinear cluster structure from HSIs by treating pixels as nodes in an undirected, weighted graph, where connections between pixels are encoded in a weight matrix  $\mathbf{W} \in \mathbb{R}^{n \times n}$  [NJW02, MM19b, MP22, PM21]. In large datasets like HSIs, edges can be restricted to the first  $N \ll n$   $\ell^2$ -nearest neighbors (i.e. Euclidean nearest neighbors) and given unit weight. In other words,  $\mathbf{W}_{ij} = 1$  if  $x_i$  is one of the  $N$  nearest neighbors of  $x_j$  or vice versa, and  $\mathbf{W}_{ij} = 0$  otherwise. Let  $\mathbf{P} = \mathbf{D}^{-1}\mathbf{W}$ , where  $\mathbf{D} \in \mathbb{R}^{n \times n}$  is the diagonal degree matrix defined by  $\mathbf{D}_{ii} = \sum_{j=1}^n \mathbf{W}_{ij}$ . The matrix  $\mathbf{P} \in \mathbb{R}^{n \times n}$  may be interpreted as the transition matrix for a Markov diffusion process on  $X$  and has a unique stationary distribution  $\pi \in \mathbb{R}^{1 \times n}$  satisfying  $\pi\mathbf{P} = \pi$  [CL06, MM19b]. Define  $\{(\lambda_i, \psi_i)\}_{i=1}^n$  to be the (right) eigenvalue-eigenvector pairs of  $\mathbf{P}$ , sorted in non-increasing order so that  $1 = \lambda_1 > |\lambda_2| > \dots > |\lambda_n| \geq 0$ . The first  $K$  eigenvectors of  $\mathbf{P}$  often concentrate on the  $K$  most coherent subgraphs in the graph underlying  $\mathbf{P}$ , making these vectors useful for clustering [NJW02].

### 2.2.1 Background on Spectral Clustering

The Spectral Clustering (SC) algorithm is the implementation of  $K$ -Means on the first  $K$  eigenvectors of  $\mathbf{P}$ , usually after a normalization step [NJW02]. Though SC can often learn latent cluster structure from datasets with nonlinear and elongated clusters, it tends to perform poorly on datasets like HSIs that contain multimodal cluster structure [NG07, MM18, MM19b].

### 2.2.2 Background on Diffusion Geometry

Diffusion distances are a family of data-dependent distance metrics that enable comparisons between points in the context of the Markov diffusion process encoded in  $\mathbf{P}$  [CL06]. Diffusion distances have been successfully used in a number of applications (e.g., in gene expression profiling [HBW<sup>+</sup>16, VDSN<sup>+</sup>18], data visualization [ZS14, MvDW<sup>+</sup>19], and molecular dynamics analysis [RZMC11, ZRMC11, CF18]). Moreover, diffusion distances have been shown to efficiently capture low-dimensional structure in HSI data, resulting in excellent clustering performance [MM18, MP22].

Define the *diffusion distance* at time  $t \geq 0$  between pixels  $x_i, x_j \in X$  [CLL<sup>+</sup>05, CL06, NLCK06] by

$$D_t(x_i, x_j) = \sqrt{\sum_{k=1}^n \frac{[(\mathbf{P}^t)_{ik} - (\mathbf{P}^t)_{jk}]^2}{\pi_k}}.$$

Diffusion distances are a nonlinear data-dependent distance metric that have a natural connection to the clustering problem [MM19b, MP22]. To see this, note that  $D_t(x_i, x_j)$  may be interpreted as the Euclidean distance between the  $i^{\text{th}}$  and  $j^{\text{th}}$  rows of  $\mathbf{P}^t$ , weighted according to  $1/\pi$ . If pixels from the same cluster share many high-weight paths of length  $t$ , but paths of length  $t$  between any two pixels from different clusters are relatively low weight, then the  $i^{\text{th}}$  and  $j^{\text{th}}$  rows of  $\mathbf{P}^t$  are expected to be nearly equal for pixels  $x_i$  and  $x_j$  from the same cluster and very different if these pixels come from different clusters. Indeed, in datasets with coherent and well-separated latent cluster structure, the maximum within-cluster diffusion distance is bounded away from the minimum between-cluster diffusion distance across a large range of  $t$  [MM19b, MP22].

Diffusion distances can be efficiently computed using the eigendecomposition of  $\mathbf{P}$  [CL06, NLCK06, CLL<sup>+</sup>05]:

$$D_t(x_i, x_j) = \sqrt{\sum_{k=1}^n \lambda_k^{2t} [(\psi_i)_k - (\psi_j)_k]^2}.$$

For  $t$  sufficiently large so that  $|\lambda_k|^{2t} \approx 0$  for  $k > \ell$ , the sum in diffusion distances can be truncated past the  $\ell^{\text{th}}$  term, yielding an accurate and efficient approximation of diffusion distances. Importantly, the relationship between diffusion distances and the eigendecomposition of  $\mathbf{P}$  indicates that diffusion distances may be interpreted as Euclidean distances after nonlinear dimensionality reduction via the following dimension-reduced mapping of the ambient space into  $\mathbb{R}^\ell$ :  $x_i \rightarrow [\lambda_1^t(\psi_1)_i \ \lambda_1^t(\psi_2)_i \ \dots \ \lambda_1^t(\psi_\ell)_i]$  [CL06, CLL<sup>+</sup>05, NLCK06]. As such, diffusion distances are related to nonlinear dimensionality reduction; e.g., locally linear embeddings [RS00], isomap [TdSL00], and Laplacian eigenmaps [BN01].

---

**Algorithm 1:** Learning by Unsupervised Nonlinear Diffusion (LUND) [MM19b]

---

- Input:**  $X$  (HSI),  $N$  (# nearest neighbors),  
 $\sigma_0$  (KDE scale),  $t$  (diffusion time),  $K$  (# clusters)  
**Output:**  $\mathcal{C}$  (clustering)
- 1 Build the KDE  $p(x)$  using  $N$   $\ell^2$ -nearest neighbors and KDE scale  $\sigma_0$ ;
  - 2 Build  $\rho_t(x)$ , where diffusion distances are computed from a KNN graph with  $N$  edges per pixel;
  - 3 Assign  $\mathcal{C}(x_{m_k}) = k$  for  $1 \leq k \leq K$ , where  $\{x_{m_k}\}_{k=1}^K$  are the  $K$  pixels maximizing  $\mathcal{D}_t(x) = p(x)\rho_t(x)$ ;
  - 4 In order of non-increasing  $p$ -value, for each unlabeled  $x \in X$ , assign the label  $\mathcal{C}(x) = \mathcal{C}(x^*)$ , where  
$$x^* = \operatorname{argmin}_{y \in X} \{D_t(x, y) \mid p(y) \geq p(x) \text{ and } \mathcal{C}(y) > 0\}.$$
- 

HSIs often encode well-defined latent multiscale cluster structure that can be learned by diffusion-based HSI clustering algorithms by varying the time parameter  $t$  in diffusion distances [PM21, MP22]. Indeed, smaller  $t$  values generally enable the detection of fine-scale local cluster structure, while larger  $t$  values enable the detection of coarse-scale global cluster structure. However, for algorithms that require  $K$  as an input,  $t$  must be tuned to correspond to the desired number of clusters. Thus, the choice of  $t$  must be carefully considered when clustering a dataset using an algorithm that relies on diffusion distances [MP22, PM21].

### 2.3 Background on the LUND Algorithm

The Learning by Unsupervised Nonlinear Diffusion (LUND) clustering algorithm (Algorithm 1) leverages the natural theoretical relationship between diffusion geometry and the clustering problem to efficiently partition datasets [CL06, MM19b, MM18]. LUND relies on two main functions to calculate cluster modes: points acting as exemplars for all underlying cluster structure. The first is a *kernel density estimate (KDE)* defined by

$$p(x) = \frac{1}{Z} \sum_{y \in NN_N(x)} \exp(-\|x - y\|_2^2 / \sigma_0^2),$$

where  $NN_N(x)$  is the set of  $N$   $\ell^2$ -nearest neighbors of  $x$  in  $X$ ,  $\sigma_0 > 0$  is a *KDE scale* controlling the interaction radius between points, and  $Z$  is a constant normalizing  $p(x)$  so that  $\sum_{y \in X} p(y) = 1$ . By construction,  $p(x)$  will be large if the pixel  $x$  is close to its  $N$   $\ell^2$ -nearest neighbors in  $X$  and small otherwise. The second function used by LUND for mode detection is

$$\rho_t(x) = \begin{cases} \max_{y \in X} D_t(x, y) & x = \operatorname{argmax}_{y \in X} p(y), \\ \min_{y \in X} \{D_t(x, y) \mid p(y) \geq p(x)\} & \text{otherwise.} \end{cases}$$

For points that are not empirical density maximizers,  $\rho_t(x)$  is the diffusion distance at time  $t$  between the pixel  $x$  and its  $D_t$ -nearest neighbor that is higher density.

Hence, the maximizers of  $\mathcal{D}_t(x) = p(x)\rho_t(x)$ , being high-density data points far in diffusion distance at time  $t$  from other high-density data points [MM19b], are reasonable choices for cluster exemplars. LUND designates the  $K$  points maximizing  $\mathcal{D}_t(x)$  as *cluster modes* and assigns these points unique labels. LUND then assigns each non-modal point (in order of non-increasing density) the label of its  $D_t$ -nearest neighbor that is higher density and already labeled. Under lax assumptions on density and the graph underlying  $\mathbf{P}$ , LUND is guaranteed to learn latent cluster structure, even in datasets with nonlinear, elongated, and/or multimodal structure. Due to its success on real and synthetic datasets, many modifications of LUND exist [MM19b, MP22, MM18, PM21, MM19c, MM19a, Mur20], some built specifically for HSI clustering [MP22, PM21, MM19c, MM18].

Though LUND has strong performance guarantees for recovering latent cluster structure on general datasets [MM19b, MP22], it may be subject to error on HSIs with highly mixed pixels. For such datasets, the spatial region corresponding to a single pixel may contain multiple materials. As such, though LUND may be equipped to segment an HSI into clusters of pixels that contain the same groups of multiple materials, it may be unable to locate individual materials within a mixed HSI.

## 2.4 Background on Spectral Unmixing

Real-world HSI data is often generated at a coarse spatial resolution; thus, pixels may correspond to spatial regions containing multiple materials [CMAC11, Win99, MSS01]. To learn latent material structure from HSIs, *spectral unmixing* algorithms decompose each pixel’s spectrum into a linear combination of *endmembers* that encode the spectral signature of materials in the scene. The coefficients of this linear combination indicate the relative *abundance* of materials within the spatial region corresponding to that pixel. Mathematically, a spectral unmixing algorithm learns  $\mathbf{U} = (u_1 \ u_2 \ \dots \ u_m)^T \in \mathbb{R}^{m \times D}$  (with rows encoding the spectral signatures of endmembers) and  $\mathbf{A} \in \mathbb{R}^{n \times m}$  (with rows encoding abundances) such that  $x_i \approx \sum_{j=1}^m \mathbf{A}_{ij} u_j$  for each  $x_i \in X$  [MSS01]. Usually,  $\mathbf{A}$  is normalized so that  $\sum_{j=1}^m \mathbf{A}_{ij} = 1$  for each  $i$ ; hence, abundances are data-dependent features storing estimates for the relative frequency of materials in pixels. The *purity* of  $x_i \in X$ , defined by  $\eta(x_i) = \max_{1 \leq i \leq m} \mathbf{A}_{ij}$  [CP21], will be large if the spatial region corresponding to  $x_i$  is highly homogeneous (i.e., containing predominantly just one material) and small otherwise. As such, pixel purity and spectral unmixing may be used to aid in the unsupervised clustering of HSIs [CP21, GKP14, KDP12].

Spectral unmixing has become an important tool within hyperspectral imagery, prompting its usage in a number of applications; e.g., image reconstruction [WFG<sup>+</sup>18], noise reduction [CMR13], and anomaly detection [QWG<sup>+</sup>18, MYW18]. The importance of spectral unmixing in remote sensing has motivated the development of many algorithms for this task [BDPCV<sup>+</sup>13]. Geometric methods for spectral unmixing estimate endmembers by searching for endmembers that form a simplex of minimal volume, subject to a constraint that at least some nearly pure pixels exist within the observed HSI pixels [CWLO06, Nev99, BKG95, Boa93, CCHM09, AG21, BDPCV<sup>+</sup>13, CMAC11, ND05]. For highly mixed HSIs that lack pure pixels, statistical methods may be used [BKL<sup>+</sup>04, ZG07, DMC<sup>+</sup>09, MBMDC06, TRK11]. These methods typically treat spectral unmixing as a blind source separation problem, and though they are often successful at this task, statistical algorithms are usually more computationally expensive [BDPCV<sup>+</sup>13]. Additionally, while linear spectral unmixing is well-developed and widely used in practice, some nonlinear unmixing algorithms (including relying on neural networks [GAC01, LDF11, COR11, SLP<sup>+</sup>19, ZSZ<sup>+</sup>18]) have been developed to account for nonlinear interactions between endmembers [GAC01, LDF11, SLP<sup>+</sup>19, ZSZ<sup>+</sup>18, YCI13, HADT11, CRH12, OKA18]. Nevertheless, these algorithms typically require training data or hyperparameter inputs unlike many of the linear mixing models reviewed above [BDPCV<sup>+</sup>13].

### 2.4.1 Background on the HySime Algorithm

Hyperspectral Signal Subspace Identification by Minimum Error (*HySime*) is a standard algorithm for estimating the number of materials  $m$  in  $X$  [BDN08]. HySime assumes that each  $x_i \in X$  is of the form  $x_i = y_i + \zeta_i$ , where  $y_i \in \mathbb{R}^D$  and  $\zeta_i \in \mathbb{R}^D$  model the signal and noise associated with  $x_i$ , respectively. If signal vectors are linear mixtures of  $m$  ground truth endmembers (i.e.,  $y_i = \sum_{j=1}^m \mathbf{A}_{ij} u_j$  for  $1 \leq i \leq m$ ), then the set  $\{y_i\}_{i=1}^m$  lies on a  $m$ -dimensional subspace of  $\mathbb{R}^D$ . With this motivation, HySime estimates the subspace dimension by balancing the error of projecting signal vectors  $\{y_i\}_{i=1}^n$  onto their first  $m$  principal components and the amount of noise captured by those vectors’ orthogonal space. Though other algorithms exist for estimating the number of materials in a scene using HSI data, many of these alternatives rely on hyperparameter inputs to estimate  $m$  or have large computational complexity [Cha18]. In contrast, HySime can compute a high-quality estimate using only  $X$  in just  $O(D^2 n)$  operations.

### 2.4.2 Background on the Alternating Volume Maximization

Alternating Volume Maximization (*AVMAX*) is a spectral unmixing algorithm, requiring  $m$  as a parameter, that searches for vectors  $\{u_i\}_{i=1}^m \subset \mathbb{R}^D$  that produce an  $m$ -simplex of maximal volume, subject to the constraint that each  $u_i$  lies in the convex hull of the dataset after PCA dimensionality reduction. Endmembers are optimized through multiple partial maximization procedures (i.e., keeping  $m - 1$  endmembers constant and optimizing for volume while varying the  $m^{\text{th}}$  endmember) until convergence [CMAC11]. AVMAX has recently become popular for spectral unmixing because of its strong performance guarantees and the rigor behind its optimization framework [CMAC11, BDPCV<sup>+</sup>13]. In a noiseless, linearly mixed dataset containing the optimal endmember set, if each partial maximization problem in AVMAX converges to a unique solution, AVMAX is guaranteed to converge to the optimal endmember set [CMAC11]. Moreover, AVMAX can easily be modified to make it robust to random initialization; one can run multiple replicates of AVMAX in

---

**Algorithm 2:** Diffusion and Volume maximization-based Image Clustering (D-VIC)

---

- Input:**  $X$  (HSI),  $N$  (# nearest neighbors),  
 $\sigma_0$  (KDE scale),  $t$  (diffusion time),  $K$  (# clusters)  
**Output:**  $\mathcal{C}$  (clustering)
- 1 Estimate  $m$ , the number of latent endmembers in  $X$ , using HySime [BDN08];
  - 2 Learn endmembers  $\mathbf{U} \in \mathbb{R}^{m \times D}$  using AVMAX [CMAC11] and abundances  $\mathbf{A} \in \mathbb{R}^{n \times m}$  using a nonnegative least squares solver [BDJ97];
  - 3 For each  $x \in X$ , calculate pixel purity  $\eta(x)$  and empirical density  $p(x)$ . Store  $\zeta(x) = \frac{2\bar{p}(x)\bar{\eta}(x)}{\bar{p}(x)+\bar{\eta}(x)}$ , where  $\bar{p}(x) = \frac{p(x)}{\max_{y \in X} p(y)}$  and  $\bar{\eta}(x) = \frac{\eta(x)}{\max_{y \in X} \eta(y)}$ ;
  - 4 Build  $d_t(x)$ , where diffusion distances are computed from a KNN graph with  $N$  edges per pixel;
  - 5 Assign  $\mathcal{C}(x_{m_k}) = k$  for  $1 \leq k \leq K$ , where  $\{x_{m_k}\}_{k=1}^K$  are the  $K$  pixels maximizing  $\mathcal{D}_t(x) = \zeta(x)d_t(x)$ ;
  - 6 In order of non-increasing  $\zeta(x)$ , for each unlabeled  $x \in X$ , assign  $x$  the label  $\mathcal{C}(x^*)$ , where  $x^* = \operatorname{argmin}_{y \in X} \{D_t(x, y) \mid \zeta(y) \geq \zeta(x) \text{ and } \mathcal{C}(y) > 0\}$ .
- 

parallel and choose the endmember set with largest volume. Once endmembers are learned, abundances can be computed using a nonnegative least squares solver  $(\mathbf{A}_{i1} \ \mathbf{A}_{i2} \ \dots \ \mathbf{A}_{im}) = \operatorname{argmin}_{\mathbf{a} \in \mathbb{R}^m} \|\mathbf{x}_i - \sum_{j=1}^m \mathbf{a}_j \mathbf{u}_j\|_2^2$  for each  $x_i \in X$  [BDJ97].

### 3 Diffusion and Volume maximization-based Image Clustering

In highly mixed HSIs, any one pixel may correspond to a spatial region that contains many materials. Thus, even state-of-the-art algorithms for unsupervised material discrimination may perform poorly on mixed HSIs, failing to recover clusterings that can be linked to materials within the scene. Algorithms that do not directly incorporate a spectral unmixing step into their labeling may assign clusters that correspond to groups of materials rather than clusters corresponding to individual materials. Thus, additional improvements are needed to improve HSI clustering algorithms for material discrimination on highly mixed images.

This section introduces the *Diffusion and Volume maximization-based Image Clustering (D-VIC)* algorithm (Algorithm 2) for unsupervised material discrimination of HSIs. To learn material abundances, D-VIC first performs a spectral unmixing step: decomposing the HSI by learning the number of endmembers  $m$  using HySime [BDN08], implementing AVMAX with that  $m$  value to learn endmembers [CMAC11], and calculating abundances and purity through a nonnegative least squares solver [BDJ97]. D-VIC then estimates empirical density using a KDE [RL14, MM18, MM19b].

To locate pixels that are both high-density and indicative of an underlying material, D-VIC calculates

$$\zeta(x) = \frac{2\bar{p}(x)\bar{\eta}(x)}{\bar{p}(x)+\bar{\eta}(x)},$$

where  $\bar{p}(x) = \frac{p(x)}{\max_{y \in X} p(y)}$  and  $\bar{\eta}(x) = \frac{\eta(x)}{\max_{y \in X} \eta(y)}$ . Thus,  $\zeta(x)$  returns the harmonic mean of  $p(x)$  and  $\eta(x)$ , which are normalized so that density and purity are approximately at the same scale. By construction,  $\zeta(x) \approx 1$  only at high-density, high-purity pixels  $x$ . In contrast, if a pixel  $x$  is either low-density or low-purity, then  $\zeta(x)$  will be small. Importantly,  $\zeta(x)$  downweights mixed pixels that, though high-density, correspond to a spatial region containing many materials. Thus, points with large  $\zeta$ -values will correspond to pixels that are modal (due to their high empirical density) and representative of just one material in the scene (due to their high pixel purity).

D-VIC uses the following function to incorporate diffusion geometry into its procedure for selecting cluster modes:

$$d_t(x) = \begin{cases} \max_{y \in X} D_t(x, y) & x = \operatorname{argmax}_{y \in X} \zeta(y), \\ \min_{y \in X} \{D_t(x, y) \mid \zeta(y) \geq \zeta(x)\} & \text{otherwise.} \end{cases}$$

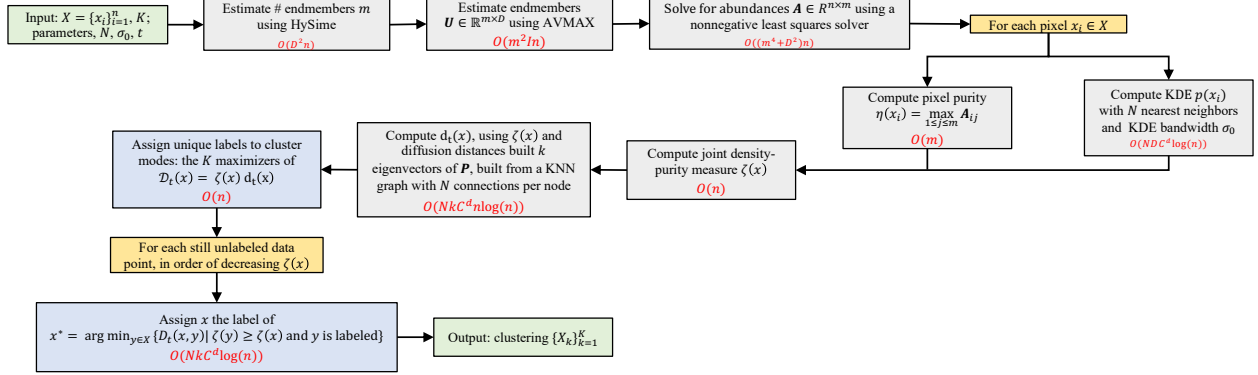


Figure 2: Diagram of the D-VIC clustering algorithm. The computational complexity of each step is colored in red. Note that all steps are quasilinear with respect to  $n$ , implying that D-VIC scales well to large HSI datasets.

Thus, a pixel will have a large  $d_t$ -value if it is far in diffusion distance at time  $t$  from its  $D_t$ -nearest neighbor of higher density and pixel purity. D-VIC assigns modal labels to the  $K$  points maximizing of  $\mathcal{D}_t(x) = d_t(x)\zeta(x)$ , which are high-density, high-purity pixels far in diffusion distance at time  $t$  from other high-density, high-purity pixels.

After labeling cluster modes, D-VIC labels non-modal points according to their  $D_t$ -nearest neighbor of higher  $\zeta(x)$ -value that is already labeled. Importantly, though this non-modal labeling is similar to the one used in LUND, D-VIC downweights low-purity pixels through  $\zeta(x)$  in its non-modal labeling. Thus, pixel purity is incorporated in all stages of the D-VIC algorithm through  $\zeta(x)$ . D-VIC is provided in Algorithm 2, and a schematic is provided in Figure 2.

### 3.1 Computational Complexity

This section considers the computational complexity of D-VIC. The computational complexity of the HySime algorithm is  $O(D^2 n)$  operations [BDN08], whereas the computational complexity of spectral unmixing using AVMAX and a standard nonnegative least squares solver [BDJ97] is  $O((D^2 + m^4 + m^2 I)n)$  operations, where  $I$  is the number of AVMAX partial maximizations [CMAC11]. We assume that nearest neighbor searches are performed using *cover trees*: an indexing data structure that enables logarithmic nearest neighbor searches [BKL06]. To see this, define the *doubling dimension* of  $X$  by  $d = \log_2(c)$ , where  $c > 0$  is the smallest value for which any ball  $B_p(p, r) = \{q \in X \mid \|p - q\| \leq r\}$  can be covered by  $c$  balls of radius  $r/2$ . If the spectral signatures of pixels in  $X \subset \mathbb{R}^D$  have doubling dimension  $d$ , a search for the  $N$   $\ell^2$ -nearest neighbors of each HSI pixel using cover trees has computational complexity  $O(NDC^d n \log(n))$ , where  $C$  is a constant independent of  $n$ ,  $D$ ,  $N$ , and  $d$ . Thus, if  $\mathbf{W}$  is constructed using cover trees [BKL06] with  $N$  nearest neighbors, and  $O(1)$  eigenvectors of  $\mathbf{P}$  are used to calculate diffusion distances, then the computational complexity of D-VIC is  $O((D^2 + m^4 + m^2 I)n + NDC^d n \log(n))$  [MM19b, BKL06].

So long as the spatial dimensions of the scene captured by an HSI are not changed, we expect that  $m$  (the expected number of materials within the scene) will be constant with respect to the number of samples  $n$ . Similarly, numerical simulations have shown that, if  $m$  remains constant as the number of samples increases, then  $I$  tends to grow only slightly [CMAC11]. If  $m = O(1)$  and  $I = O(\log(n))$  with respect to  $n$ , then the complexity of D-VIC reduces to  $O(NDC^d n \log(n))$ .

### 3.2 Comparison to Related HSI Clustering Algorithms

In this section, D-VIC is compared theoretically against related graph-based HSI clustering algorithms; empirical comparisons appear in Section 4.

### 3.2.1 Symmetric Nonnegative Matrix Factorization

Nonnegative matrix factorization (NMF)-based clustering algorithms typically assume that each cluster in a latent clustering can be represented using just a single basis vector [GKP14, CHNP04, KDP12]. Though this assumption holds for datasets sampled from a union of affine spaces, it can fail on HSIs, which often contain nonlinear structure [ZWL<sup>+</sup>16, KDP12]. Rather than directly decomposing the pixels in  $X$  as is done in other NMF-based clustering algorithms [GKP14], the symmetric NMF (SymNMF) algorithm decomposes the weight matrix  $\mathbf{W}$  using the following optimization:  $\mathbf{H}^* = \operatorname{argmin}_{\mathbf{H} \in \mathbb{R}^{n \times \kappa}} \|\mathbf{W} - \mathbf{H}\mathbf{H}^T\|_F^2$  subject to  $\mathbf{H}_{ij} \geq 0$ . Assuming data points from the same cluster are weighted highly in the graph, but points from different clusters have low edge weights, the matrix  $\mathbf{H}^*$  will naturally encode latent (possibly nonlinear) cluster structure in  $X$ . After performing its NMF step, SymNMF labels points according to the largest entries in  $\mathbf{H}^*$ :  $\mathcal{C}(x_i) = \operatorname{argmax}_{1 \leq j \leq K} \mathbf{H}_{ij}^*$ .

D-VIC and SymNMF are similar in that they both rely on the decomposition of a matrix encoding a graph representation of  $X$  to learn underlying (possibly nonlinear) latent cluster structure. Nevertheless, there are key differences that may lead SymNMF to erroneous clusterings. SymNMF does not directly incorporate empirical density or pixel purity into its labeling, leaving it prone to error on datasets containing multimodal cluster structure or HSIs with mixed pixels. In contrast, D-VIC upweights high-density, high-purity points within its mode selection, making it robust to error on these problematic classes of data. Moreover, though SymNMF has been shown to perform well on real HSI data [KDP12], its cluster assignments tend to be sensitive to the initialization of  $\mathbf{H}$ .

### 3.2.2 KNN-SSC

The *K-Nearest Neighbors-based Sparse Subspace Clustering (KNN-SSC)* algorithm modifies SC to learn the best locality-preserving low-rank representation of the data [LLY<sup>+</sup>12, ZWL<sup>+</sup>16]. More precisely, KNN-SSC finds  $(\mathbf{Z}^*, \mathbf{E}^*) \in \mathbb{R}^{n \times n} \times \mathbb{R}^{n \times D}$  minimizing  $\|\mathbf{Z}\|_* + \lambda \|\mathbf{E}\|_{2,1}$  ( $\lambda > 0$  is a regularization parameter) subject to the following constraints: (i)  $\mathbf{X} = \mathbf{Z}\mathbf{X} + \mathbf{E}$  so that data points are expressed as linear combinations of other data points; (ii)  $\mathbf{1}\mathbf{Z} = \mathbf{1}$  so that coefficients in these linear combinations sum to 1; and (iii)  $\mathbf{Z}_{ij} > 0$  if and only if  $x_j$  is one of the  $N$   $\ell^2$ -nearest neighbors of  $x_i$ . SC is then implemented using the weight matrix  $\mathbf{W} = \frac{1}{2}(|\mathbf{Z}^*| + |\mathbf{Z}^*|^T)$  to produce the KNN-SSC clustering of  $X$  [NJW02, ZWL<sup>+</sup>16].

The KNN-SSC and D-VIC algorithms are similar in that they both rely on a linear unmixing step to extract additional information from the dataset [LLY<sup>+</sup>12, ZWL<sup>+</sup>16, CP21]. However, KNN-SSC does not incorporate data density into its clustering procedure, leaving it prone to error on data with multimodal cluster structure [NG07, MM19b, MP22]. Moreover, while KNN-SSC relies on the minimization of a convex objective function subject to linear constraints, there are at least two main difficulties in the KNN-SSC optimization [ZWL<sup>+</sup>16]. First, though the objective function  $\|\mathbf{Z}\|_* + \lambda \|\mathbf{E}\|_{2,1}$  is convex, it is not smooth. Second, the constraint that  $\mathbf{Z}_{ij} > 0$  if and only if  $x_i$  and  $x_j$  are  $\ell^2$ -nearest neighbors significantly restricts the domain. These complications may yield a much slower convergence, even if the graph provided is superior. A final concern is that KNN-SSC scales quadratically with  $n$  in storage costs. As such, KNN-SSC may not be suitable for clustering large HSI datasets.

### 3.2.3 Learning by Unsupervised Nonlinear Diffusion

We remark that, for any one cluster, there may be multiple reasonable choices for cluster modes: pixels that are exemplary of underlying cluster structure. In LUND, cluster modes are selected to be high-density pixels that are far in diffusion distance from other high-density pixels [MM19b, MM18]. However, not all high-density pixels necessarily correspond to underlying material structure. A maximizer of  $p(x)$  could, for example, correspond to a spatial region containing a group of commonly co-occurring materials (rather than a single material). By weighting pixel purity and density equally, D-VIC avoids selecting such a pixel as cluster mode; thus, D-VIC modes will be both indicative of underlying material structure and modal, making these points better exemplars of underlying material structure than the modes selected by LUND.

This section illustrates the key difference between LUND and D-VIC by implementing both algorithms on a simple dataset (visualized in Figure 3) built to illustrate the idealized scenario where D-VIC outperforms LUND due to its incorporation of pixel purity. This dataset was generated by sampling  $n = 5000$  points from an equilateral triangle in  $\mathbb{R}^2$  centered at the origin with edge length  $\sqrt{2}$ ; the  $K = 3$  vertices of this

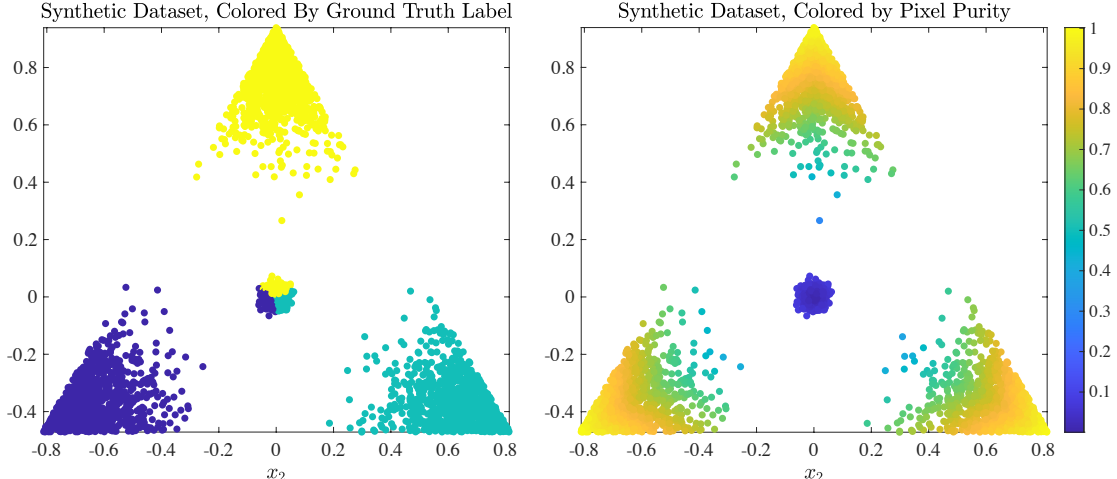


Figure 3: Ground truth labels and pixel purity of synthetic dataset. Notice that empirical density maximizers near the origin are also lowest-purity data points.

triangle served as ground truth endmembers. We sampled 1000 data points from a Gaussian distribution with a standard deviation of 0.175 centered at each endmember, keeping only the samples lying within the convex hull of the ground truth endmember set. In addition, 2000 data points were sampled from a Gaussian distribution with zero-mean and a smaller standard deviation of 0.0175. As such, high-purity points indicative of latent material structure were also relatively low-density, and density maximizers were engineered so to not be indicative of latent material structure. Each point was assigned a ground truth label corresponding to its highest-abundances ground truth endmember.

For both LUND and D-VIC, overall accuracy (OA), defined to be the fraction of correctly labeled pixels, was optimized for across the same grid of relevant hyperparameter values (see Appendix A). The optimal clusterings and their corresponding OA values are provided in Figure 4. These numerical results illustrate a fundamental limitation of relying solely on empirical density to select cluster modes in spectrally mixed HSI data. Because empirical density maximizers are not representative of underlying material structure in this synthetic dataset, LUND is unable to discriminate data points within the high-density, low-purity region near the origin, resulting in poor performance and an OA of 0.739. In contrast, D-VIC downweights high-density points that are not also high-purity and therefore selects points that are more representative of the dataset’s underlying material structure as cluster modes. As a result, D-VIC correctly separates the high-density, low-purity region into three segments, yielding a substantially higher OA of 0.905, a difference of 0.166 when compared to LUND.

## 4 Numerical Experiments

This section contains numerical results indicating the efficacy of D-VIC. Classical and state-of-the-art clustering algorithms were implemented on three real HSI datasets described in Section 4.1. Classical algorithms D-VIC was compared against include  $K$ -Means [FHT01],  $K$ -Means applied to the first principal components of the HSI ( $K$ -Means+PCA) [FHT01], and GMM applied to first principal components of the HSI (GMM+PCA) [FHT01]. D-VIC was also compared against several state-of-the-art HSI clustering algorithms: SC [NJW02], SymNMF [KDP12], KNN-SSC [AG21, ZWL<sup>+</sup>16], and LUND [MM19b, MM18] (see Sections 2.2.1, 2.3, and 3.2).

In all experiments, the number of clusters was set equal to the ground truth  $K$ . We clustered the entire image but discarded unlabeled pixels when comparing clusterings to the ground truth labels. Comparisons were made using OA and Cohen’s  $\kappa$  coefficient:  $\kappa = \frac{OA - p_e}{1 - p_e}$ , where  $p_e$  is the probability that a clustering agrees with the ground truth labels by chance. OA was optimized for across hyperparameters ranging a grid of relevant values for each algorithm (see Appendix A). We report the median OA across 100 trials for  $K$ -Means, GMM, SymNMF, and D-VIC to account for the stochasticity associated with random initial

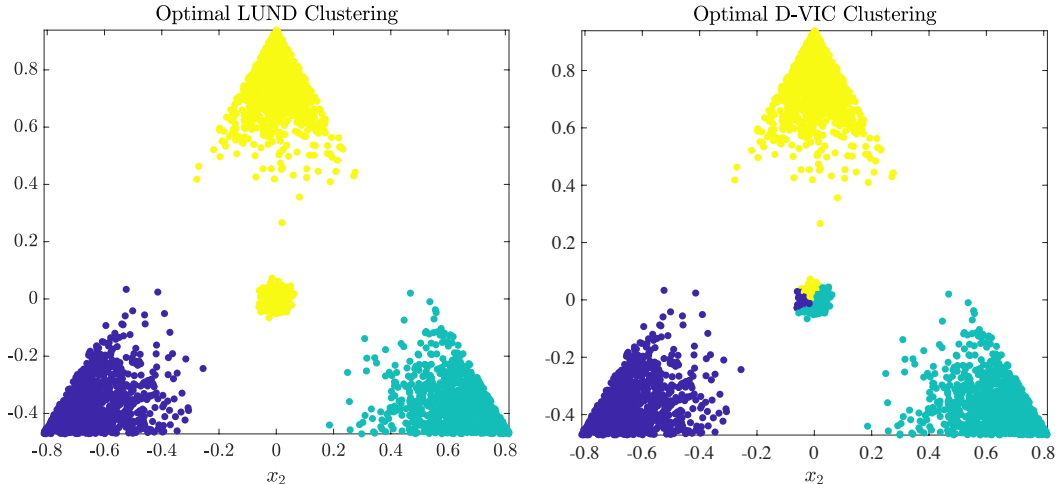


Figure 4: Optimal LUND (OA = 0.739) and D-VIC (OA = 0.905) clusterings of the synthetic dataset (Figure 3).

conditions. Diffusion distances were computed using only the first 10 eigenvectors of  $\mathbf{P}$  in LUND and D-VIC. For D-VIC, AVMAX was implemented 100 times in parallel, and the endmember set that formed the largest-volume simplex was selected for later cluster analysis. Numerical experiments can be replicated at <https://github.com/sampolk/D-VIC>.

#### 4.1 Description of Benchmark HSI Datasets

To illustrate the efficacy of D-VIC, we analyzed three publicly available, real HSIs often used as benchmarks for new HSI clustering algorithms; see Figure 5 and the descriptions below. Water absorption bands were discarded, and pixel spectra were standardized before analysis.

1. *Salinas A* (Figure 5a) was recorded by the Airborne Visible/Infrared Imaging Spectrometer (AVIRIS) sensor over farmland in Salinas Valley, California, USA in 1998 at a spatial resolution of 1.3 m. Spectral signatures, ranging in recorded wavelength from 380 nm to 2500 nm across 224 spectral bands, were recorded across  $83 \times 86$  pixels ( $n = 7138$ ). Gaussian noise (with mean 0 and standard deviation =  $10^{-7}$ ) was added to each pixel to differentiate two pixels with identical spectral signatures. The Salinas A scene contains  $K = 6$  ground truth classes corresponding to crop types.
2. *Jasper Ridge* (Figure 5b) was recorded by the AVIRIS sensor over the Jasper Ridge Biological Preserve, California, USA in 1989 at a spatial resolution of 5 m. Spectral signatures, ranging in recorded wavelength from 380 nm to 2500 nm across 224 spectral bands, were recorded across spatial dimensions of  $100 \times 100$  pixels ( $n = 10000$ ). The Jasper Ridge scene contains  $K = 4$  ground truth endmembers: road, soil, water, and trees. Ground truth labels were recovered by selecting the material of highest ground truth abundance for each pixel.
3. *Indian Pines* (Figure 5c) was recorded by the AVIRIS sensor over farmland in northwest Indiana, USA in 1992 at a low spatial resolution of 20 m. Spectral signatures, ranging in recorded wavelength from 400 nm to 2500 nm across 224 spectral bands, were recorded across spatial dimensions of  $145 \times 145$  pixels ( $n = 21025$ ). The Indian Pines scene contains  $K = 16$  ground truth classes (e.g., crop types and manufactured structures) as well as many unlabeled pixels.

#### 4.2 Performance Comparisons

This section compares clusterings produced by D-VIC against those of related algorithms (Table 1). On each of the three benchmark HSIs analyzed, D-VIC produces a clustering that is closer to the ground truth labels than those produced by related algorithms. The Indian Pines dataset (Fig. 5c) is expected to be challenging

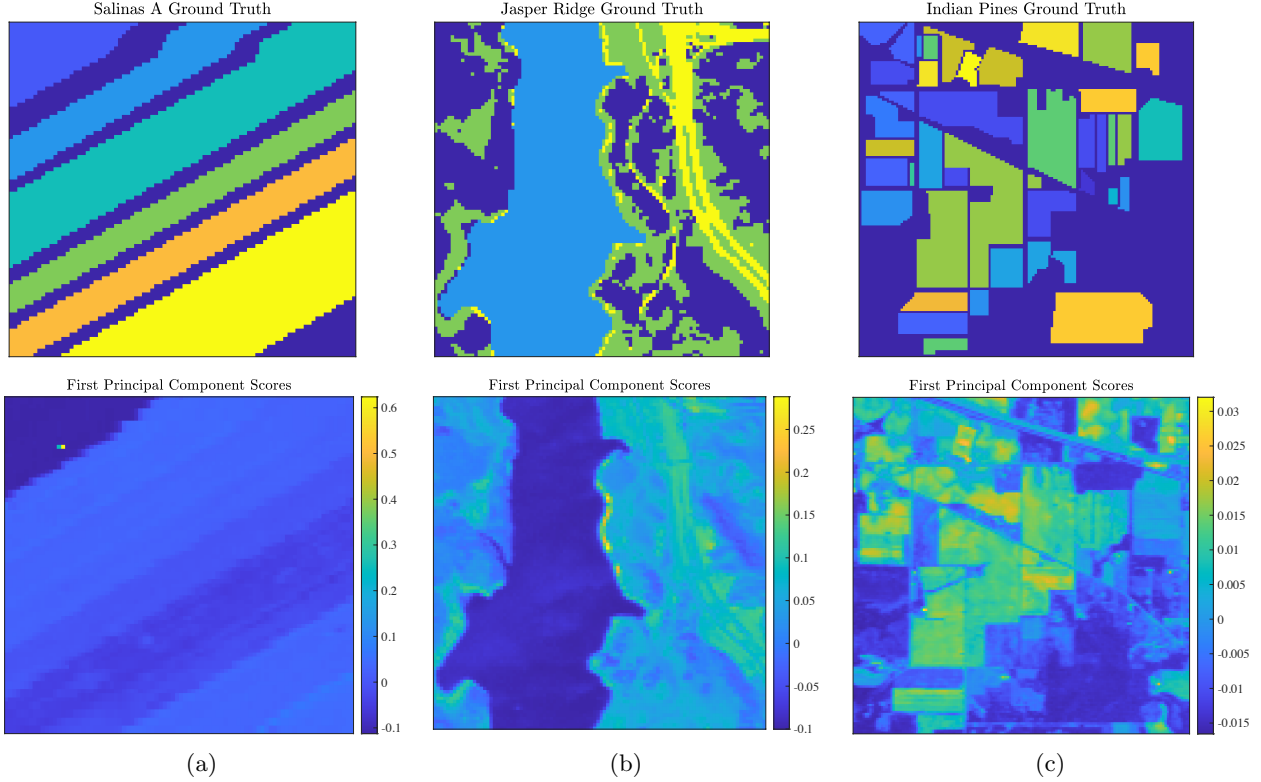


Figure 5: Ground truth labels and first principal component scores for the real benchmark HSIs analyzed in this article.

because pixels from the same class exist in multiple segments of the image, and the size of ground truth clusters varies substantially across the  $K = 16$  classes. Nevertheless, D-VIC achieves higher performance than all other algorithms on this challenging dataset. Notably, though all other algorithms (including state-of-the-art algorithms, such as LUND) achieve  $\kappa$ -statistics in the same narrow range of 0.298 to 0.316, D-VIC achieves a substantially higher  $\kappa$ -statistic of 0.350. As such, the incorporation of pixel purity in D-VIC enables superior detection even in this difficult setting.

As visualized in Figure 6, D-VIC achieved nearly perfect recovery of the ground truth labels for Salinas A. Most notably, though all comparison methods erroneously separate the ground truth cluster indicated in yellow in Figure 5a (corresponding to 8-week maturity romaine), D-VIC correctly groups the pixels in this cluster, resulting in a performance that was 0.089 higher in OA and 0.110 in  $\kappa$  than the that of LUND, its closest competitor in Table 1. As such, downweighting high-density points that are not also exemplary of the latent material structure improves not only modal, but also non-modal labeling. Moreover, what error

	Salinas A		Jasper Ridge		Indian Pines	
	OA	$\kappa$	OA	$\kappa$	OA	$\kappa$
<i>K</i> -Means	0.764	0.703	0.784	0.703	0.383	0.315
<i>K</i> -Means+PCA	0.764	0.703	0.785	0.703	0.382	<b>0.316</b>
GMM+PCA	0.611	0.512	0.789	0.701	0.364	0.292
SC	0.834	0.797	0.760	0.670	0.382	0.314
SymNMF	0.828	0.791	0.662	0.542	0.365	0.304
KNN-SSC	0.844	0.809	0.726	0.629	0.371	0.308
LUND	<b>0.887</b>	<b>0.860</b>	<b>0.815</b>	<b>0.737</b>	<b>0.404</b>	0.312
D-VIC	<b>0.976</b>	<b>0.970</b>	<b>0.865</b>	<b>0.805</b>	<b>0.445</b>	<b>0.350</b>

Table 1: Performances of D-VIC and related algorithms on benchmark HSIs. Highest and second-highest performances are bolded and italicized respectively. The median OA across 100 trials is reported for *K*-Means, *K*-Means+PCA, GMM+PCA, SC, SymNMF, and D-VIC. D-VIC offers substantially higher performance on all datasets evaluated.

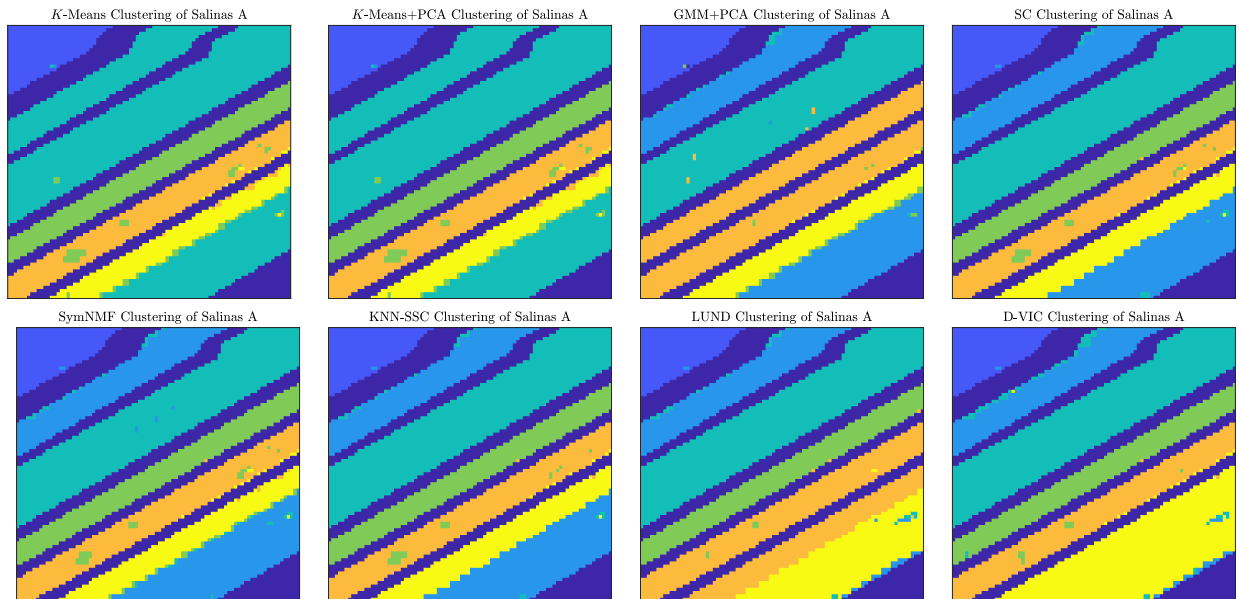


Figure 6: Comparison of clusterings produced by D-VIC and related algorithms on the Salinas A HSI. Unlike any comparison method, D-VIS correctly groups pixels corresponding to 8-week maturity romaine (indicated in yellow), resulting in near-perfect recovery of the ground truth labels.

does exist in the D-VIC clustering of Salinas A could likely be remedied through spatial regularization or post-processing smoothing [MM19c, Mur20].

D-VIC similarly achieved much higher performance than related state-of-the-art graph-based clustering algorithms on Jasper Ridge (as visualized in Figure 7). This difference in performance was substantially driven by superior separation of the classes indicated in dark blue (corresponding to tree cover) and green (corresponding to soil) in Figure 5b. Indeed, though LUND groups most tree cover pixels with soil pixels in Figure 7, D-VIC correctly separates much of the latent structure for this class. The difference between LUND’S and D-VIC’s clusterings indicates that the pixels corresponding to the tree cover class, though lower density than pixels corresponding to the soil class, have relatively high pixel purity.

### 4.3 Robustness to Hyperparameter Selection

This section analyzes the robustness of D-VIC’s performance to hyperparameter selection. For each node in a grid of  $(N, \sigma_0)$ , D-VIC was implemented 50 times, and the median OA value across these 50 trials was stored. Performance degraded as  $N$  increased substantially past 100, and such a choice is not advised. In Figure 8, we visualize how the performance of D-VIC varies with  $N$  and  $\sigma_0$ . The relative nominal values in the range of  $\sigma_0$  reflect that pixels from the HSIs analyzed in this article are relatively close to their  $\ell^2$ -nearest neighbors on average. As is described in Appendix A, the range of  $\sigma_0$  used for each grid search is data-dependent, ranging the distribution of  $\ell^2$ -distances between pixel spectra and their 1000  $\ell^2$ -nearest neighbors. Thus, the ranges indicated in Figure 8 cover the relevant values of  $\sigma_0$ .

It is clear from Figure 8 that D-VIC is capable of achieving high performance across a broad range of hyperparameters on each HSI. Thus, given little hyperparameter tuning, D-VIC is likely to output a partition that is competitive with clusterings reported in Table 1. Figure 8 also motivates recommendations for hyperparameter selection to optimize the OA of D-VIC. Larger datasets (e.g., Indian Pines) tend to require larger values of  $N$  for D-VIC to achieve high OA, corresponding with recommendations in the literature that  $N$  should grow logarithmically with  $n$  [MM19b]. Additionally, for datasets with high-purity material classes (e.g., Salinas A), D-VIC achieves highest OA using large  $\sigma_0$ . This reflects that, as  $\sigma_0$  increases, the KDE  $p(x)$  becomes more constant across the HSI and  $\zeta(x) \approx \eta(x)$ . Since purity is an excellent indicator of material class structure for Salinas A, D-VIC becomes better able to recover the latent material structure with larger  $\sigma_0$ .

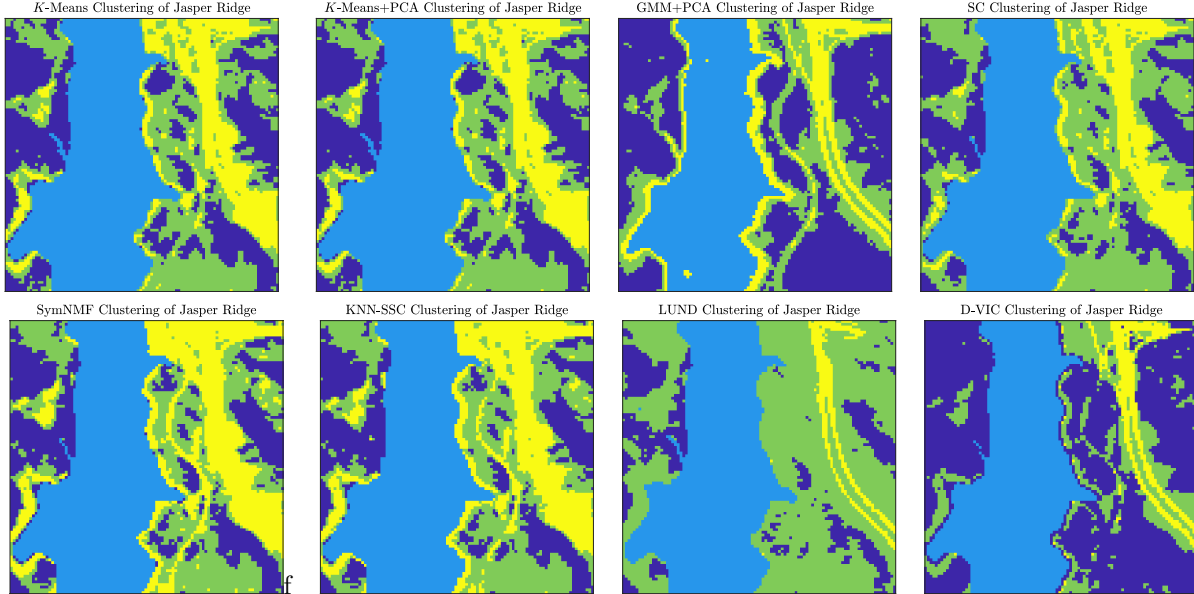


Figure 7: Comparison of clusterings produced by D-VIC and related algorithms on the Jasper Ridge HSI. D-VIC outperforms all other algorithms, largely due to superior discrimination of the pixels corresponding to tree and soil classes (indicated in dark blue and green respectively).

We also analyze the robustness of D-VIC’s performance to the selection of the diffusion time parameter  $t$ . Using the optimal values of  $N$  and  $\sigma_0$ , D-VIC was evaluated 100 times at  $t$ -values ranging  $\{10, 20, \dots, 200\}$ . Figure 9, which visualizes the results of this analysis, indicates D-VIC achieves high OA values across a broad range of  $t$ ; for each  $t \in [90, 200]$ , D-VIC outputs a clustering with OA equal to or very close to those reported in Table 1. These results indicate that D-VIC is well-equipped to provide high-quality clusterings given little or no tuning of  $t$ . Indeed, a simple choice of  $t = 100$  works extremely well across all datasets.

#### 4.4 Runtime Analysis

This section compares runtimes of the algorithms implemented in Section 4.2, where hyperparameters were set to be those which produced the results in Table 1. All experiments were run in MATLAB on the same environment: a macOS Big Sur system with an 8-core Apple<sup>®</sup> M1<sup>™</sup> Processor and 8 GB of RAM. Each

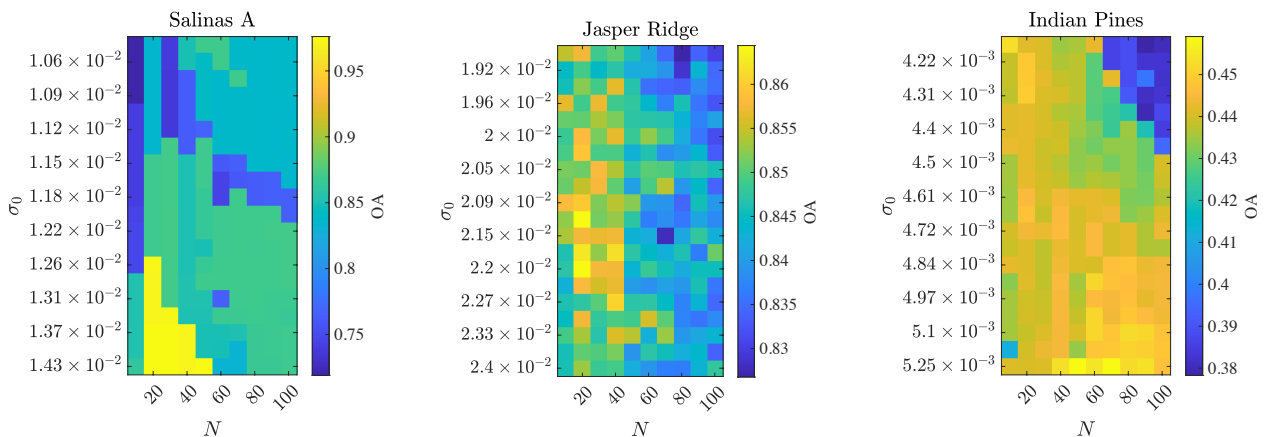


Figure 8: Visualization of D-VIC’s median OA across 50 trials as hyperparameters  $N$  and  $\sigma_0$  are varied. D-VIC achieves high performance across a large set of hyperparameters.

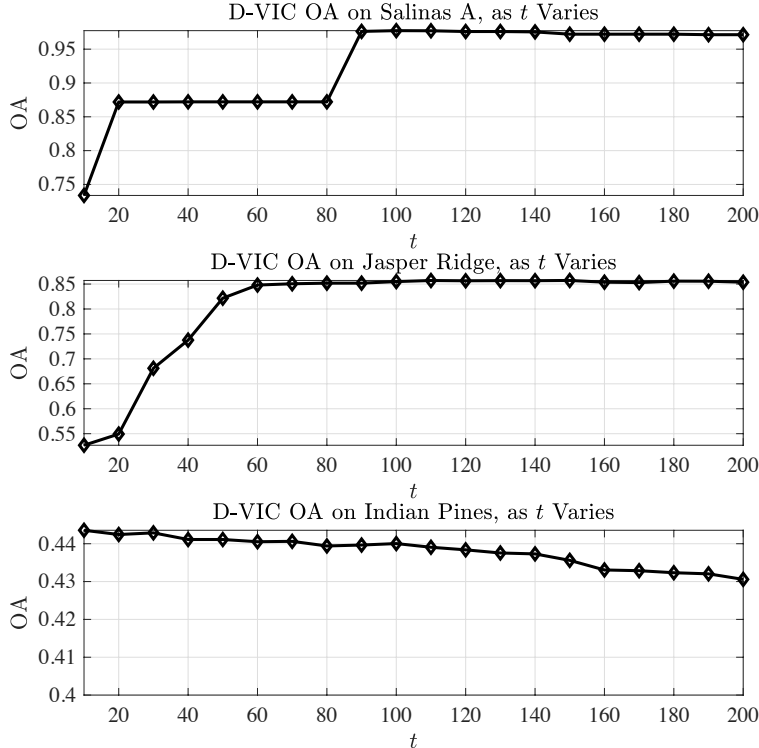


Figure 9: Analysis of D-VIC’s performance as  $t$  varies across  $[10, 200]$ . Values are the median OA across 100 implementations of D-VIC with the optimal  $N$  and  $\sigma_0$  values. Generally,  $t$  appears to have little impact on the OA of D-VIC, and D-VIC achieves performances comparable to those reported in Table 1 across  $t \in [90, 200]$ , uniformly across all data sets.

core had a processor base frequency of 3.20 GHz. Runtimes are provided in Table 2. All classical algorithms have smaller runtimes than D-VIC, but the performances reported in Table 1 for these algorithms are substantially less than those reported for D-VIC. On the other hand, though KNN-SSC and SymNMF achieve performances competitive to D-VIC, unlike D-VIC, these algorithms appear to scale poorly to large datasets. Finally, D-VIC outperforms LUND at the cost of only a small increase in runtime (associated with an additional spectral unmixing step).

## 5 Conclusion

This article introduces the *D-VIC clustering algorithm* for unsupervised material discrimination in HSIs. D-VIC assigns modal labels to high-density, high-purity pixels within the HSI that are far in diffusion distance from other high-density, high-purity pixels [CMAC11, MM19b, CP21]. We have argued that these *cluster modes* are highly indicative of underlying material structure, leading to more interpretable and accurate

	Salinas A	Jasper Ridge	Indian Pines
<i>K</i> -Means	0.04	0.10	1.04
<i>K</i> -Means+PCA	0.10	0.14	0.58
GMM+PCA	0.13	0.23	2.19
SC	1.82	3.15	14.54
SymNMF	3.50	4.42	48.29
KNN-SSC	4.11	7.91	103.05
LUND	2.35	4.14	14.74
D-VIC	4.95	7.64	23.70

Table 2: Runtimes (seconds) of D-VIC and related algorithms. D-VIC achieves runtimes comparable to state-of-the-art algorithms and scales well to the larger Indian Pines dataset.

clusterings than those produced by related algorithms [MM18, MM19b]. Indeed, numerical experiments presented in Section 4 show that incorporating pixel purity into D-VIC results in clusterings closer to the ground truth labels on three benchmark real HSI datasets of varying sizes and complexities. As such, D-VIC is equipped to perform efficient material discrimination on broad ranges of mixed HSI datasets.

Future work includes modifying the spectral unmixing step in D-VIC to account for nonlinear mixing of endmembers. Linear endmember extraction is computationally inexpensive [BDN08, CMAC11, BDJ97], and it results in strong performance in D-VIC, but recent years have brought significant advances in algorithms for the nonlinear spectral unmixing of HSIs [CRH12, HADT11, YCI13]. Modifying the spectral unmixing step in D-VIC may improve performance, especially for HSIs in which assumptions on linear mixing do not hold [CRH12, HADT11, YCI13].

Additionally, much of the error in D-VIC’s clusterings may be corrected through by incorporating spatial information into its labeling. Such a modification of D-VIC may improve performance on datasets with spatially homogeneous clusters [MM19c, PM21, FTB<sup>+</sup>12, GBU13, FLD<sup>+</sup>15, TBC09, MSB07]. Moreover, it is likely that varying the diffusion time parameter  $t$  in D-VIC may enable the detection of multiple scales of latent cluster structure: a problem we would like to consider further in future work [MP22, PM21, GKP14]. Finally, we expect D-VIC may be modified for *active learning*, wherein ground truth labels for a small number of carefully selected pixels are queried and propagated across the image [MM19a, Mur20].

## Acknowledgment

The US National Science Foundation partially supported this research through grants NSF-DMS 1912737, NSF-DMS 1924513, and NSF-CCF 1934553. We thank C. Schönlieb, M. S. Kotzagiannidis, and D. Coomes for conversations that aided in the development of D-VIC. In addition, we thank N. Gillis, D. Kuang, H. Park, C. Ding, M. Abdolali, D. Kun, and I. Gerg for making code for HySime [BDN08], AVMAX [GK22, CMAC11], SymNMF [KDP12], and KNN-SSC [AG21] publicly available.

## A Hyperparameter Optimization

This section describes the hyperparameter optimization performed to generate Table 1. The parameter grids used for each algorithm are summarized in Table 3. For  $K$ -Means+PCA and GMM+PCA, we clustered the first  $z$  principal components of the HSI, where  $z$  was chosen so that 99% of the variation in the HSI was maintained after PCA dimensionality reduction. Thus,  $K$ -Means,  $K$ -Means+PCA, and GMM+PCA required no hyperparameter inputs. For stochastic algorithms with hyperparameter inputs (SC, SymNMF, and D-VIC), we optimized for the median OA across 10 trials at each node in the hyperparameter grids described below.

All graph-based algorithms relied on adjacency matrices built from sparse KNN graphs. The number of nearest neighbors was optimized for each algorithm across  $\mathcal{N}$ : an exponential sampling of the set [10, 900]. KNN-SSC’s regularization parameter was set to  $\lambda = 10$ , motivated by prior work with this parameter [AG21]. In addition to  $N$ , LUND and D-VIC clustering algorithms also require the KDE scale  $\sigma_0 > 0$  and diffusion time  $t$  as input. In our grid searches,  $\sigma_0$  ranged  $\mathcal{D}$ : a sampling of the distribution of  $\ell^2$ -distances between

Algorithm	Param. 1 Grid	Param. 2 Grid	Param. 3 Grid
$K$ -Means	—	—	—
$K$ -Means+PCA	—	—	—
GMM+PCA	—	—	—
SC [NJW02]	$N \in \mathcal{N}$	—	—
SymNMF [KDP12]	$N \in \mathcal{N}$	—	—
KNN-SSC [AG21, ZWL <sup>+</sup> 16]	$N \in \mathcal{N}$	$\lambda = 10$	—
LUND [MM19b]	$N \in \mathcal{N}$	$\sigma_0 \in \mathcal{D}$	$t \in \mathcal{T}$
D-VIC	$N \in \mathcal{N}$	$\sigma_0 \in \mathcal{D}$	$t \in \mathcal{T}$

Table 3: Hyperparameter grids for algorithms. The number of nearest neighbors  $N$  took values in  $\mathcal{N}$ : an exponential sampling of the set [10, 900]. The set  $\mathcal{D}$  contains  $\ell^2$ -distances between data points and their 1000  $\ell^2$ -nearest neighbors. The set  $\mathcal{T}$  is an exponential sampling of the diffusion process:  $\mathcal{T} = \{0, 1, 2, \dots, 2^2, \dots, 2^T\}$ . A “—” indicates a lack of a hyperparameter input.

data points and their 1000  $\ell^2$ -nearest neighbors. Similarly, both LUND and D-VIC were implemented at time steps  $t \in \mathcal{T} = \{0, 1, 2, 2^2, \dots, 2^T\}$ , where  $T = \lceil \log_2[\log_{\lambda_2(\mathbf{P})}(\frac{2 \times 10^{-5}}{\min(\pi)})] \rceil$ . Searches end at time  $t = 2^T$  because  $\max_{x,y \in X} D_t(x,y) \leq 10^{-5}$  for  $t \geq 2^T$ . For each dataset, we chose the  $t \in \{0, 1, 2, 2^2, \dots, 2^T\}$  resulting in maximal OA. We selected  $t = 2^5$  for Salinas A,  $t = 2^7$  for Jasper Ridge, and  $t = 0$  for Indian Pines. As noted in Section 4.3, D-VIC is quite robust to this choice of parameter.

## References

- [AG21] Maryam Abdolali and Nicolas Gillis. Beyond linear subspace clustering: A comparative study of nonlinear manifold clustering algorithms. *Comput Sci Rev*, 42:1574–0137, 2021.
- [AMR10] E Adam, O Mutanga, and D Rugege. Multispectral and hyperspectral remote sensing for identification and mapping of wetland vegetation: a review. *Wetl Ecol Manag*, 18(3):281–296, 2010.
- [BAF05] Charles M Bachmann, Thomas L Ainsworth, and Robert A Fusina. Exploiting manifold geometry in hyperspectral imagery. *IEEE Trans Geosci Remote Sens*, 43(3):441–454, 2005.
- [BDJ97] Rasmus Bro and Sijmen De Jong. A fast non-negativity-constrained least squares algorithm. *J Chemom*, 11(5):393–401, 1997.
- [BDN08] José M Bioucas-Dias and José MP Nascimento. Hyperspectral subspace identification. *IEEE Trans Geosci Remote Sens*, 46(8):2435–2445, 2008.
- [BDPCV<sup>+</sup>13] José M Bioucas-Dias, Antonio Plaza, Gustavo Camps-Valls, Paul Scheunders, Nasser Nasrabadi, and Jocelyn Chanussot. Hyperspectral remote sensing data analysis and future challenges. *IEEE Geosci Remote Sens Mag*, 1(2):6–36, 2013.
- [BKG95] J W Boardman, F A Kruse, and R O Green. Mapping target signatures via partial unmixing of AVIRIS data. 1995.
- [BKL<sup>+</sup>04] M Berman, H Kiveri, R Lagerstrom, A Ernst, R Dunne, and J F Huntington. ICE: A statistical approach to identifying endmembers in hyperspectral images. *IEEE Trans Signal Process*, 42(10):2085–2095, 2004.
- [BKL06] Alina Beygelzimer, Sham Kakade, and John Langford. Cover trees for nearest neighbor. In *Proc ICML*, pages 97–104, 2006.
- [BN01] M Belkin and Partha Niyogi. Laplacian eigenmaps and spectral techniques for embedding and clustering. In *Proc NeurIPS*, volume 14, 2001.
- [Boa93] Joseph W Boardman. Automating spectral unmixing of AVIRIS data using convex geometry concepts. In *Proc Annu JPL Airborne Geosci Workshop*, volume 1, pages 11–14, 1993.
- [CCHM09] T Chan, C Chi, Y Huang, and W Ma. A convex analysis-based minimum-volume enclosing simplex algorithm for hyperspectral unmixing. *IEEE Trans Signal Process*, 57(11):4418–4432, 2009.
- [CCM14] N D Cahill, W Czaja, and D W Messinger. Schroedinger eigenmaps with nondiagonal potentials for spatial-spectral clustering of hyperspectral imagery. In *Proc SPIE XX*, volume 9088, pages 27–39. SPIE, 2014.
- [CF18] W Chen and A L Ferguson. Molecular enhanced sampling with autoencoders: On-the-fly collective variable discovery and accelerated free energy landscape exploration. *J of Comput Chem*, 39(25):2079–2102, 2018.
- [Cha18] Chein Chang. A review of virtual dimensionality for hyperspectral imagery. *IEEE J Sel Top Appl Earth Obs Remote Sens*, 11(4):1285–1305, 2018.

- [CHNP04] M Catral, Lixing Han, Michael Neumann, and Robert J Plemmons. On reduced rank nonnegative matrix factorization for symmetric nonnegative matrices. *Linear Algebra Appl*, 393:107–126, 2004.
- [CKS10] J G P W Clevers, L Kooistra, and M E Schaepman. Estimating canopy water content using hyperspectral remote sensing data. *Int J Appl Earth Obs Geoinf*, 12(2):119–125, 2010.
- [CL06] Ronald R Coifman and Stéphane Lafon. Diffusion maps. *Appl and Comput Harm Anal*, 21(1):5–30, 2006.
- [CLL<sup>+</sup>05] Ronald R Coifman, Stephane Lafon, Ann B Lee, Mauro Maggioni, Boaz Nadler, Frederick Warner, and Steven W Zucker. Geometric diffusions as a tool for harmonic analysis and structure definition of data: Diffusion maps. *Proc Natl Acad Sci USA*, 102(21):7426–7431, 2005.
- [CMAC11] Tsung Chan, Wing Ma, ArulMurugan Ambikapathi, and Chong Chi. A simplex volume maximization framework for hyperspectral endmember extraction. *IEEE Trans Geosci Remote Sens*, 49(11):4177–4193, 2011.
- [CMR13] Daniele Cerra, Rupert Müller, and Peter Reinartz. Noise reduction in hyperspectral images through spectral unmixing. *IEEE Geosci Remote Sens Lett*, 11(1):109–113, 2013.
- [COR11] Adam S Charles, Bruno A Olshausen, and Christopher J Rozell. Learning sparse codes for hyperspectral imagery. *IEEE Journal of Selected Topics in Signal Processing*, 5(5):963–978, 2011.
- [CP21] Kangning Cui and Robert J Plemmons. Unsupervised classification of AVIRIS-NG hyperspectral images. In *Proc WHISPERS*, pages 1–5. IEEE, 2021.
- [CRH12] J Chen, C Richard, and Paul Honeine. Nonlinear unmixing of hyperspectral data based on a linear-mixture/nonlinear-fluctuation model. *IEEE Trans Signal Process*, 61(2):480–492, 2012.
- [CVMZ07] G Camps-Valls, T V B Marsheva, and D Zhou. Semi-supervised graph-based hyperspectral image classification. *IEEE Trans Geosci Remote Sens*, 45(10):3044–3054, 2007.
- [CWLO06] C Chang, C Wu, W Liu, and Y Ouyang. A new growing method for simplex-based endmember extraction algorithm. *IEEE Trans Geosci Remote Sens*, 44(10):2804–2819, 2006.
- [DBG08] M Dalponte, L Bruzzone, and D Gianelle. Fusion of hyperspectral and lidar remote sensing data for classification of complex forest areas. *IEEE Trans Geosci Remote Sens*, 46(5):1416–1427, 2008.
- [DMC<sup>+</sup>09] N Dobigeon, S Moussaoui, M Coulon, J Tournieret, and A O Hero. Joint Bayesian endmember extraction and linear unmixing for hyperspectral imagery. *IEEE Trans Signal Process*, 57(11):4355–4368, 2009.
- [EGVL<sup>+</sup>12] Gerda J Edelman, Edurne Gaston, Ton G Van Leeuwen, PJ Cullen, and Maurice CG Aalders. Hyperspectral imaging for non-contact analysis of forensic traces. *Forensic Sci Int*, 223(1-3):28–39, 2012.
- [Eis12] Michael Theodore Eismann. *Hyperspectral remote sensing*. SPIE, 2012.
- [FHT01] Jerome Friedman, Trevor Hastie, and Robert Tibshirani. *The elements of statistical learning*, volume 1. Springer Series in Statistics, 2001.
- [FLD<sup>+</sup>15] Leyuan Fang, Shutao Li, Wuhui Duan, Jinchang Ren, and Jón Atli Benediktsson. Classification of hyperspectral images by exploiting spectral-spatial information of superpixel via multiple kernels. *IEEE Trans Geosci Remote Sens*, 53(12):6663–6674, 2015.

- [FTB<sup>+</sup>12] Mathieu Fauvel, Yuliya Tarabalka, Jon Atli Benediktsson, Jocelyn Chanussot, and James C Tilton. Advances in spectral-spatial classification of hyperspectral images. *Proceedings of the IEEE*, 101(3):652–675, 2012.
- [GAC01] K J Guilfoyle, M L Althouse, and C Chang. A quantitative and comparative analysis of linear and nonlinear spectral mixture models using radial basis function neural networks. *IEEE Trans Geosci Remote Sens*, 39(10):2314–2318, 2001.
- [GBU13] Pedram Ghamisi, Jon Atli Benediktsson, and Magnus Orn Ulfarsson. Spectral–spatial classification of hyperspectral images based on hidden markov random fields. *IEEE Trans Geosci Remote Sens*, 52(5):2565–2574, 2013.
- [GJC<sup>+</sup>14] Y Gao, R Ji, P Cui, Q Dai, and G Hua. Hyperspectral image classification through bilayer graph-based learning. *IEEE Trans Image Process*, 23(7):2769–2778, 2014.
- [GK22] Isaac Gerg and David Kun. Hyperspectral toolbox. <https://github.com/davidkun/HyperSpectralToolbox>, 2022.
- [GKP14] Nicolas Gillis, Da Kuang, and Haesun Park. Hierarchical clustering of hyperspectral images using rank-two nonnegative matrix factorization. *IEEE Trans Geosci Remote Sens*, 53(4):2066–2078, 2014.
- [GPC<sup>+</sup>17] Pedram Ghamisi, Javier Plaza, Yushi Chen, Jun Li, and Antonio J Plaza. Advanced spectral classifiers for hyperspectral images: A review. *IEEE Geosci Remote Sens Mag*, 5(1):8–32, 2017.
- [HADT11] Abderrahim Halimi, Yoann Altmann, Nicolas Dobigeon, and Jean-Yves Tourneret. Nonlinear unmixing of hyperspectral images using a generalized bilinear model. *IEEE Trans Geosci Remote Sens*, 49(11):4153–4162, 2011.
- [HBW<sup>+</sup>16] L Haghverdi, M Büttner, F A Wolf, F Buettner, and F J Theis. Diffusion pseudotime robustly reconstructs lineage branching. *Nat methods*, 13(10):845–848, 2016.
- [HMW03] A Hirano, M Madden, and R Welch. Hyperspectral image data for mapping wetland vegetation. *Wetl*, 23(2):436–448, 2003.
- [HYV20] Benjamin David Haeffele, Chong You, and Rene Vidal. A critique of self-expressive deep subspace clustering. In *International Conference on Learning Representations*, 2020.
- [JWC<sup>+</sup>20] Jianxin Jia, Yueming Wang, Jinsong Chen, Ran Guo, Rong Shu, and Jianyu Wang. Status and application of advanced airborne hyperspectral imaging technology: A review. *Infr Phys Technol*, 104:103115, 2020.
- [JWZ<sup>+</sup>17] J Jia, Y Wang, X Zhuang, Y Yao, S Wang, D Zhao, R Shu, and J Wang. High spatial resolution shortwave infrared imaging technology based on time delay and digital accumulation method. *Infr Phys Technol*, 81:305–312, 2017.
- [KDP12] Da Kuang, Chris Ding, and Haesun Park. Symmetric nonnegative matrix factorization for graph clustering. In *Proc SDM12*, pages 106–117. SIAM, 2012.
- [LDF11] G A Licciardi and F Del Frate. Pixel unmixing in hyperspectral data by means of neural networks. *IEEE Trans Geosci Remote Sens*, 49(11):4163–4172, 2011.
- [LLY<sup>+</sup>12] Guangcan Liu, Zhouchen Lin, Shuicheng Yan, Ju Sun, Yong Yu, and Yi Ma. Robust recovery of subspace structures by low-rank representation. *IEEE Trans Pattern Anal Mach Intell*, 35(1):171–184, 2012.
- [LQL<sup>+</sup>21] K Li, Y Qin, Q Ling, Y Wang, Z Lin, and W An. Self-supervised deep subspace clustering for hyperspectral images with adaptive self-expressive coefficient matrix initialization. *IEEE J Sel Top Appl Earth Obs Remote Sens*, 14:3215–3227, 2021.

- [LSR15] Valero Laparrerc and Raúl Santos-Rodriguez. Spatial/spectral information trade-off in hyperspectral images. In *Proc IGARSS*, pages 1124–1127. IEEE, 2015.
- [MBMDC06] S Moussaoui, D Brie, A Mohammad-Djafari, and C Carteret. Separation of non-negative mixture of non-negative sources using a bayesian approach and MCMC sampling. *IEEE Trans Signal Process*, 54(11):4133–4145, 2006.
- [MM18] James M Murphy and Mauro Maggioni. Unsupervised clustering and active learning of hyperspectral images with nonlinear diffusion. *IEEE Trans Geosci Remote Sens*, 57(3):1829–1845, 2018.
- [MM19a] Mauro Maggioni and James M Murphy. Learning by active nonlinear diffusion. *Found Data Sci*, 1(3):271, 2019.
- [MM19b] Mauro Maggioni and James M Murphy. Learning by unsupervised nonlinear diffusion. *J Mach Learn Res*, 20(160):1–56, 2019.
- [MM19c] James M Murphy and Mauro Maggioni. Spectral–spatial diffusion geometry for hyperspectral image clustering. *IEEE Geosci Remote Sens Lett*, 17(7):1243–1247, 2019.
- [MP22] James M. Murphy and Sam L. Polk. A multiscale environment for learning by diffusion. *Appl Comput Harm Anal*, 57:58–100, 2022.
- [MSB07] A Mohan, G Sapiro, and E Bosch. Spatially coherent nonlinear dimensionality reduction and segmentation of hyperspectral images. *IEEE Geosci Remote Sens Lett*, 4(2):206–210, 2007.
- [MSS01] Dimitris Manolakis, Christina Siracusa, and Gary Shaw. Hyperspectral subpixel target detection using the linear mixing model. *IEEE Trans Geosci Remote Sens*, 39(7):1392–1409, 2001.
- [Mur20] James M Murphy. Spatially regularized active diffusion learning for high-dimensional images. *Pattern Recognit Lett*, 135:213–220, 2020.
- [MvDW<sup>+</sup>19] K R Moon, D van Dijk, Z Wang, S Gigante, D B Burkhardt, W S Chen, K Yim, A van den Elzen, M J Hirn, and R R Coifman. Visualizing structure and transitions in high-dimensional biological data. *Nat Biotechnol*, 37(12):1482–1492, 2019.
- [MYW18] Dandan Ma, Yuan Yuan, and Qi Wang. Hyperspectral anomaly detection via discriminative feature learning with multiple-dictionary sparse representation. *Remote Sens*, 10(5):745, 2018.
- [ND05] José MP Nascimento and José MB Dias. Vertex component analysis: A fast algorithm to unmix hyperspectral data. *IEEE Trans Geosci Remote Sens*, 43(4):898–910, 2005.
- [Nev99] R Neville. Automatic endmember extraction from hyperspectral data for mineral exploration. In *Proc CSRS*, 1999.
- [NG07] Boaz Nadler and Meirav Galun. Fundamental limitations of spectral clustering. In *Proc NeurIPS*, pages 1017–1024, 2007.
- [NJW02] Andrew Y Ng, Michael I Jordan, and Yair Weiss. On spectral clustering: Analysis and an algorithm. In *Proc NeurIPS*, pages 849–856, 2002.
- [NLCK06] Boaz Nadler, Stéphane Lafon, Ronald R Coifman, and Ioannis G Kevrekidis. Diffusion maps, spectral clustering and reaction coordinates of dynamical systems. *Appl Comput Harmon Anal*, 21(1):113–127, 2006.
- [NMI<sup>+</sup>20] Jakub Nalepa, Michal Myller, Yasuteru Imai, Ken-ichi Honda, Tomomi Takeda, and Marek Antoniak. Unsupervised segmentation of hyperspectral images using 3-d convolutional autoencoders. *IEEE Geosci Remote Sens Lett*, 17(11):1948–1952, 2020.

- [NYC15] A Nguyen, J Yosinski, and J Clune. Deep neural networks are easily fooled: High confidence predictions for unrecognizable images. In *Proc IEEE CVPR*, pages 427–436, 2015.
- [OKA18] Savas Ozkan, Berk Kaya, and Gozde Bozdagi Akar. Endnet: Sparse autoencoder network for endmember extraction and hyperspectral unmixing. *IEEE Trans Geosci Remote Sens*, 57(1):482–496, 2018.
- [PM21] Sam L. Polk and James M. Murphy. Multiscale clustering of hyperspectral images through spectral-spatial diffusion geometry. In *Proc IGARSS*, pages 4688–4691, 2021.
- [PMP<sup>+</sup>11] Antonio Plaza, Gabriel Martín, Javier Plaza, Maciel Zortea, and Sergio Sánchez. Recent developments in endmember extraction and spectral unmixing. In *Opt Remote Sens*, pages 235–267. Springer, 2011.
- [Pri97] John C Price. Spectral band selection for visible-near infrared remote sensing: spectral-spatial resolution tradeoffs. *IEEE Trans Geosci Remote Sens*, 35(5):1277–1285, 1997.
- [QWG<sup>+</sup>18] Ying Qu, Wei Wang, Rui Guo, Bulent Ayhan, Chimam Kwan, Steven Vance, and Hairong Qi. Hyperspectral anomaly detection through spectral unmixing and dictionary-based low-rank decomposition. *IEEE Trans Geosci Remote Sens*, 56(8):4391–4405, 2018.
- [RCY11] K Rohe, S Chatterjee, and B Yu. Spectral clustering and the high-dimensional stochastic blockmodel. *Ann Stat*, 39(4):1878–1915, 2011.
- [RL14] Alex Rodriguez and Alessandro Laio. Clustering by fast search and find of density peaks. *Science*, 344(6191):1492–1496, 2014.
- [RS00] S T Roweis and L K Saul. Nonlinear dimensionality reduction by locally linear embedding. *Science*, 290(5500):2323–2326, 2000.
- [RZMC11] M A Rohrdanz, W Zheng, M Maggioni, and C Clementi. Determination of reaction coordinates via locally scaled diffusion map. *J Chem Phys*, 134(12):03B624, 2011.
- [SLP<sup>+</sup>19] Y Su, J Li, A Plaza, A Marinoni, P Gamba, and S Chakravorty. DAEN: Deep autoencoder networks for hyperspectral unmixing. *IEEE Trans Geosci Remote Sens*, 57(7):4309–4321, 2019.
- [SWW<sup>+</sup>20] J Sun, W Wang, X Wei, L Fang, X Tang, Y Xu, H Yu, and W Yao. Deep clustering with intraclass distance constraint for hyperspectral images. *IEEE Trans Geosci Remote Sens*, 59(5):4135–4149, 2020.
- [SZS<sup>+</sup>14] C Szegedy, W Zaremba, I Sutskever, J Bruna, D Erhan, I Goodfellow, and R Fergus. Intriguing properties of neural networks. In *Proc ICLR*, 2014.
- [TBC09] Yuliya Tarabalka, Jón Atli Benediktsson, and Jocelyn Chanussot. Spectral-spatial classification of hyperspectral imagery based on partitional clustering techniques. *IEEE Trans Geosci Remote Sens*, 47(8):2973–2987, 2009.
- [TdSL00] J B Tenenbaum, V de Silva, and J C Langford. A global geometric framework for nonlinear dimensionality reduction. *Science*, 290(5500):2319–2323, 2000.
- [TK06] S Theodoridis and K Koutroumbas. *Pattern recognition*. Elsevier, 2006.
- [TRK11] Konstantinos E Themelis, Athanasios A Rontogiannis, and Konstantinos D Koutroumbas. A novel hierarchical Bayesian approach for sparse semisupervised hyperspectral unmixing. *IEEE Trans Signal Process*, 60(2):585–599, 2011.
- [VDSN<sup>+</sup>18] D Van Dijk, R Sharma, J Nainys, K Yim, P Kathail, A J Carr, C Burdziak, K R Moon, C L Chaffer, and D Pattabiraman. Recovering gene interactions from single-cell data using data diffusion. *Cell*, 174(3):716–729, 2018.

- [WFG<sup>+</sup>18] Li Wang, Yan Feng, Yanlong Gao, Zhongliang Wang, and Mingyi He. Compressed sensing reconstruction of hyperspectral images based on spectral unmixing. *IEEE J Sel Top Appl Earth Obs Remote Sens*, 11(4):1266–1284, 2018.
- [Win99] Michael E Winter. N-FINDR: An algorithm for fast autonomous spectral end-member determination in hyperspectral data. In *Proc Imaging Spectr V*, volume 3753, pages 266–275. SPIE, 1999.
- [WNW<sup>+</sup>19] R Wang, N Nie, Z Wang, F He, and X Li. Scalable graph-based clustering with nonnegative relaxation for large hyperspectral image. *IEEE Trans Geosci Remote Sens*, 57(10):7352–7364, 2019.
- [WP17] H Wu and Saurabh Prasad. Semi-supervised deep learning using pseudo labels for hyperspectral image classification. *IEEE Trans Image Process*, 27(3):1259–1270, 2017.
- [YCI13] Naoto Yokoya, Jocelyn Chanussot, and Akira Iwasaki. Nonlinear unmixing of hyperspectral data using semi-nonnegative matrix factorization. *IEEE Trans Geosci Remote Sens*, 52(2):1430–1437, 2013.
- [YYL<sup>+</sup>18] Xiaofei Yang, Yunming Ye, Xutao Li, Raymond YK Lau, Xiaofeng Zhang, and Xiaohui Huang. Hyperspectral image classification with deep learning models. *IEEE Trans Geosci Remote Sens*, 56(9):5408–5423, 2018.
- [ZCT<sup>+</sup>17] Wei Zhu, Victoria Chayes, Alexandre Tiard, Stephanie Sanchez, Devin Dahlberg, Andrea L Bertozzi, Stanley Osher, Dominique Zosso, and Da Kuang. Unsupervised classification in hyperspectral imagery with nonlocal total variation and primal-dual hybrid gradient algorithm. *IEEE Trans Geosci Remote Sens*, 55(5):2786–2798, 2017.
- [ZG07] A Zare and P Gader. Sparsity promoting iterated constrained endmember detection in hyperspectral imagery. *IEEE Geosci Remote Sens Lett*, 4(3):446–450, 2007.
- [ZRMC11] W Zheng, M A Rohrdanz, M Maggioni, and C Clementi. Polymer reversal rate calculated via locally scaled diffusion map. *J Chem Phys*, 134(14):144109, 2011.
- [ZS14] Z Zhao and A Singer. Rotationally invariant image representation for viewing direction classification in cryo-EM. *J Struct Biol*, 186(1):153–166, 2014.
- [ZSZ<sup>+</sup>18] X Zhang, Y Sun, J Zhang, P Wu, and L Jiao. Hyperspectral unmixing via deep convolutional neural networks. *IEEE Geosci Remote Sens Lett*, 15(11):1755–1759, 2018.
- [ZWL<sup>+</sup>16] Liansheng Zhuang, Jingjing Wang, Zhouchen Lin, Allen Y Yang, Yi Ma, and Nenghai Yu. Locality-preserving low-rank representation for graph construction from nonlinear manifolds. *Neurocomputing*, 175:715–722, 2016.